THE ASTROPHYSICAL JOURNAL, 323:756–765, 1987 December 15

H_2O MASERS IN CIRCUMSTELLAR ENVELOPES

ADAIR P. LANE,[1] K. J. JOHNSTON,[2] P. F. BOWERS,[2,3] J. H. SPENCER,[2] AND P. J. DIAMOND[4]
Received 1986 October 31; accepted 1987 June 19

ABSTRACT

The spatial structure of H_2O maser emission at 22.235 GHz for 12 late-type variable stars has been measured with a resolution of 0".07. The H_2O maser regions of Mira variables range from 9 or less to 108 AU in total extent, while those of supergiant long-period variables are 300–720 AU in extent. The size of the H_2O maser regions of giants and supergiants is correlated with the stellar mass-loss rate. Several of the observed sources show evidence for nonspherical geometry in the distribution of their H_2O maser emission.

The Mira variable IK Tau exhibits ~31 maser features over a total velocity range of 41 km s^{-1}. The spatial distribution of these features appears to be consistent with two spherical shells of radii 25 and 59 AU, both expanding at a velocity of 15.5 km s^{-1} from the star. We also find evidence for density inhomogeneities and turbulent motions in the envelopes of both IK Tau and R Aql.

Subject headings: interferometry — masers — stars: circumstellar shells — stars: long-period variables

I. INTRODUCTION

The association of OH, H_2O, and SiO maser emission with oxygen-rich red giants and supergiants provides a useful probe of the spatial structure and kinematics of their circumstellar envelopes and of the mass-loss process in these stars. Radio interferometric observations of these masers indicate that OH masers in the ground rotational transitions are operating in the outermost regions (500–10^4 AU) of the envelope where the circumstellar gas is expanding at nearly constant velocity, while H_2O and SiO masers are associated with regions closer to the star where turbulent motions and gas acceleration may be important. Available interferometry data for OH, as well as single-dish maps of CO at millimeter wavelengths, provide evidence for spherical symmetry in the outermost regions of the envelope for a number of late-type stars (e.g., Bowers, Johnston, and Spencer 1983; Herman *et al.* 1985; Wannier *et al.* 1979). Far less is known about the geometry and velocity structure of the warm, inner regions. VLBI observations of SiO maser emission at 43 GHz toward the M supergiant VX Sgr indicate these masers are located in an expanding spherical shell of radius ~50 AU, while the SiO masers toward the Mira variable R Cas are distributed over an elongated region ~20 AU in size (Lane 1982, 1984). High-resolution radio observations of H_2O masers have likewise been limited to a few sources. VLBI measurements of H_2O masers in several late-type giant stars were made by Spencer *et al.* (1979). In all but one of the stars, only a single H_2O maser feature was detected; the two features detected in W Hya were separated by less than 0".04 (4 AU). Lower resolution observations of H_2O masers have been made toward two Mira variables (R Aql and RR Aql), the SRb semiregular variable RX Boo, and the supergiant NML Cyg by Johnston, Spencer, and Bowers (1985, hereafter JSB) using the VLA, and toward VX Sgr (Chapman and Cohen 1986) and VY CMa (Diamond *et al.* 1987*b*) using MERLIN. These observations indicate sizes for the H_2O maser regions of less than ~50 AU for the giant stars and 400–720 AU for the three supergiants.

Additional clarification of the circumstances associated with stellar H_2O maser emission is provided by the collisional pumping scheme recently presented by Cooke and Elitzur (1985). Their model suggests a correlation between the radius of the maser emission region and the stellar mass-loss rate. Based on available data for OH, H_2O, and SiO, Bowers (1985) also suggested that the size of the maser region increases with increasing mass-loss rate for OH and possibly for H_2O and SiO. Thus spatial measurements of the extent of maser emission may provide another method for determining mass-loss rates, in addition to those obtained from CO and infrared measurements.

We have observed the H_2O maser emission from 11 Mira variables and one supergiant with the VLA in order to characterize the spatial extent and kinematics of the maser regions and to examine the possible connection between maser region size and stellar mass-loss rate. In this paper we present the results for the 11 giant stars and summarize data from the literature for other sources. Our results for the supergiant S Per are discussed in more detail in a separate paper in conjunction with VLBI observations of this source (Diamond *et al.* 1987*a*).

II. OBSERVATIONS

The observations were obtained on 1983 October 6–7, using the Very Large Array of the National Radio Astronomy Observatory.[5] The antennas were in the A-configuration, with baseline lengths ranging from 0.6 to 37 km, yielding a synthesized beamwidth of 0".07. The number of antennas available in the spectral line mode of this instrument varied from 14 to 17. The data were obtained in right circular polarization with a total bandwidth of 3.125 MHz (42.2 km s^{-1}). For each star the bandpass was centered at or near the stellar radial velocity. Sixty-four channels were used with on-line Hanning weighting, resulting in a velocity resolution of 1.3 km s^{-1}. The flux density scale was established by assuming a flux density of 43 Jy for 3C 84 at 22,235.080 MHz.

Each star was observed for ~15 minutes at each of 5 or 6 hr angles to provide a distribution of observations in the (u, v)-

[1] Astronomy Department, Boston University.
[2] E. O. Hulburt Center for Space Research, Naval Research Laboratory.
[3] Sachs/Freeman Associates, Bowie, Maryland.
[4] Max-Planck-Institute für Radioastronomie, Bonn, West Germany.

[5] The National Radio Astronomy Observatory is operated by Associated Universities, Inc., under contract with the National Science Foundation.

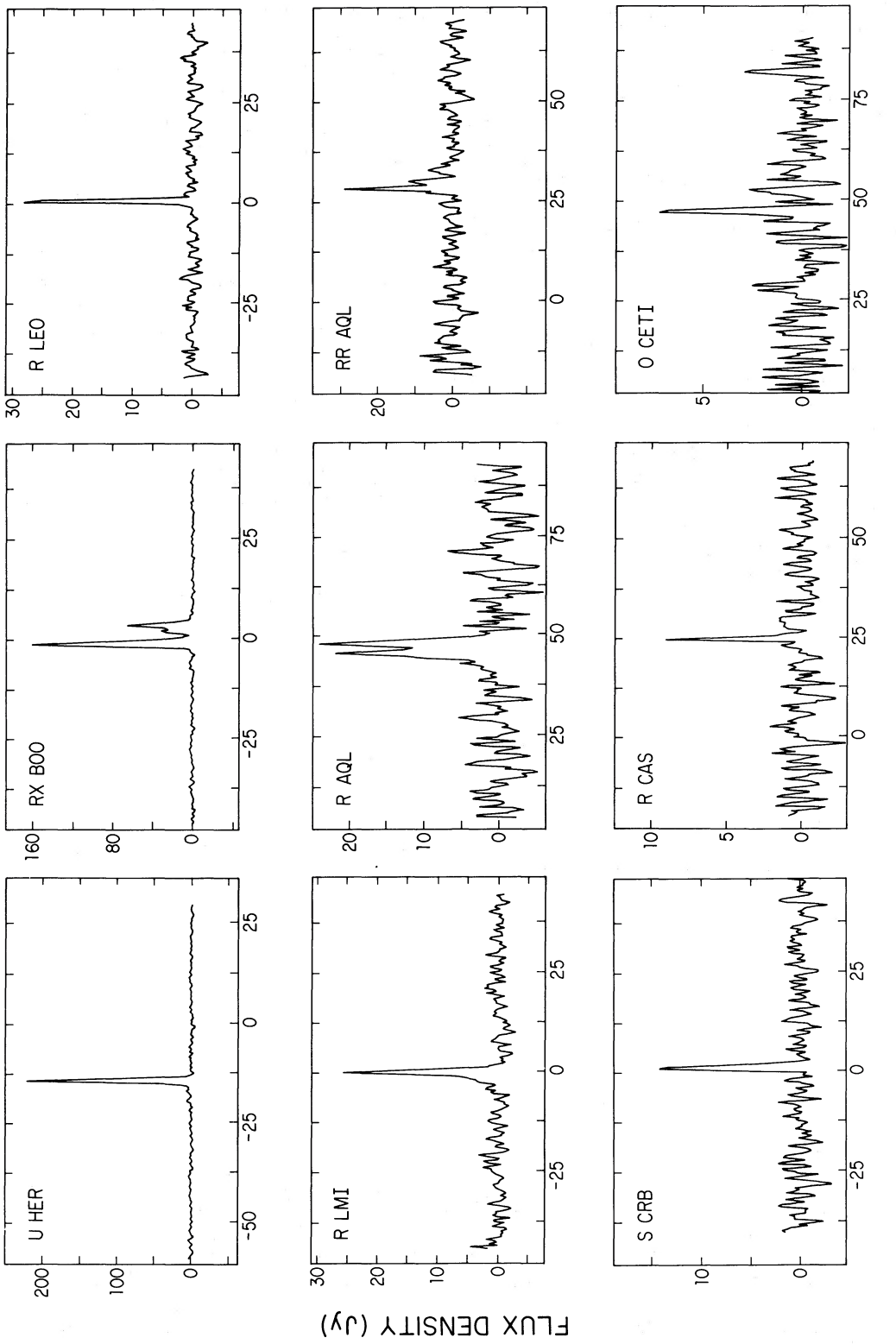

FIG. 1.—H_2O maser spectra for nine stars obtained with the Onsala 20 m telescope between 1983 October 5–9. Line frequency is 22235.08 MHz and the velocities are with respect to the LSR. The spectral resolution is 0.4 km s^{-1}. Most of the stars have simple spectra; the more complex spectrum of IK Tau is shown in Fig. 3*a*.

plane. Each stellar observation was followed by a 5 minute observation of a nearby calibrator. The data were calibrated in the standard manner using the nearby calibrators to establish the system phase and amplitude. The phase stability during these observations proved to be poor, probably due to atmospheric effects. The Astronomical Image Processing System (AIPS) was used to produce maps of each spectral channel where signal was detected. It was necessary to use self-calibration algorithms in AIPS to obtain reasonable maps. In several cases the data were of such poor quality that a point source in the center of the map was used for the initial model. After a few iterations, the self-calibration converged. The absolute positional accuracy of the maps cannot be estimated due to the use of the self-calibration algorithm, but the relative positional accuracy of the spectral features of individual stars is of order 0".005.

Single-dish H_2O spectra for the observed stars (with the exception of W Hya) were measured with the 20 m telescope of the Onsala Space Observatory between 1983 October 5–9. The total bandwidth was 7.5 MHz with 256 channels yielding a resolution of 29 kHz or 0.4 km s^{-1}. A second-order baseline was removed from the spectra and atmospheric attenuation was estimated from measurements of the local relative humidity. The flux density scale was established by observation of 3C 84 which was assumed to have a flux density of 43 Jy. The absolute flux density scale is estimated to be accurate to 20%. The spectra of nine of the stars are shown in Figure 1. The spectrum of IK Tau is presented in § IV, while the data for S Per are reported in Diamond *et al.* (1987*a*).

III. RESULTS

The spectra of most of the stars were fairly simple at the time of these measurements as the single-dish spectra of Figure 1 indicate. Consequently, it is not surprising that most of the stars (eight of the 11 reported here) displayed emission from only a few (one to four) maser "spots" distributed over one or two beamwidths. Several sources, including R Aql (see § V), RX Boo, U Her, and S CrB, show evidence for elongated rather than spherical maser regions, while spherical shell structure appears to be present in IK Tau (see § IV). All of the features shown in the single-dish spectra were detected with the VLA. The flux densities summed from the VLA maps agree to within 20% with those measured with the Onsala telescope.

Table 1 gives a summary of data for 15 stars for which the H_2O emission has been mapped with interferometric techniques (this paper; JSB; Chapman and Cohen 1986; Diamond *et al.* 1987*a*, *b*). Three sources have been observed at more than one epoch as indicated in column (2). Column (3) lists the number of discrete maser "features" which appear on the maps. (In several cases, this number could not be determined precisely due to spatial blending of features). The angular diameter of the H_2O region (col. [4]) refers to the maximum angular separation between observed maser spots (which may differ slightly from twice the mean radius of the maser region as determined by fitting kinematic models to the data). The distances used to convert the angular sizes to linear sizes are given in column (5) with references in column (8). The stars are listed in order of increasing linear diameter of the H_2O maser region

TABLE 1

CHARACTERISTIC SIZES OF H_2O MASER REGIONS

Star (1)	Number of Epochs Observed (2)	Number of Spots on Map (3)	Angular Diameter of Region (4)	Distance (pc) (5)	Linear Diameter of Region (AU) (6)	Mass-Loss Rate ($\times 10^{-6}$ $M_\odot$ yr^{-1}) (7)	References (8)	(9)	(10)
Giants:									
o Ceti	1	1	≤0".1	85	≤9	0.8	1	2	3
R Leo	1	1	≤0.1	162	≤16	0.03	1	2	3
R Cas	1	1	≤0.1	243	≤24	0.6	1	2	3
W Hya	1	~3	0.31	100	31	1.8	4	2	5
RX Boo	2	2–3	0.14	225	32	0.4	6	2, 7	3
S CrB	1	2–3	0.09	375	34	4.0	1	2	5
R LMi	1	2–3	0.15	335	50	0.7	1	2	8
R Aql	3	~13	0.33	172	57	0.8	1	2, 7	5
U Her	1	3–4	0.15	390	59	2.6	1	2	5
RR Aql	3	several	0.16	560	90	0.7	1	2, 7	9
IK Tau	1	~31	0.40	270	108	5.1	10	2	3
Supergiants:									
S Per	1	~24	0.13	2300	300	27.	11	12	5
VY CMa	1	many	0.29	1350	395	80.	13	14	15
VX Sgr	1	~15	0.32	1500	480	195.	16	17	18
NML Cyg	1	5–6	0.40	1800	720	150.	19	7	8

NOTES.—Col. (8) = reference for distance. Col. (9) = reference for linear diameter of H_2O maser region. Col. (10) = reference for mass-loss rate.

REFERENCES.—(1) Bowers and Hagen 1984, using the period-luminosity-spectral class relationship of Celis 1980, 1981. (2) This paper. (3) Knapp and Morris 1985, from CO emission. (4) Wilson *et al.* 1972. (5) Gehrz and Woolf 1971, from 10 μm silicate feature. (6) Morris *et al.* 1979. (7) Johnston *et al.* 1985. (8) Knapp *et al.* 1982, from CO emission. (9) Bowers *et al.* 1983, from radius of OH maser region. (10) Hyland *et al.* 1972. (11) Humphreys 1975. (12) Diamond *et al.* 1987*a*. (13) Armandroff and Herbst 1981. (14) Diamond *et al.* 1987*b*. (15) Zuckerman and Dyck 1986, from CO emission. (16) Lockwood and Wing 1982. (17) Chapman and Cohen 1986. (18) Diamond *et al.* 1987*a*, from infrared luminosity and envelope expansion velocity. (19) Bowers *et al.* 1983.

(col. [6]). The diameters of the H_2O regions range from 9 or less to 108 AU for the giant stars and from 300 to 720 AU for the supergiant stars. The estimated stellar mass-loss rates are given in column (7) with references and method of determination given in the footnotes. Mass-loss rates from the literature have been scaled to the distances listed in Table 1, when appropriate.

In cases where more than one estimate of the mass-loss rate is available, we have preferentially selected values determined from observations of CO emission. Such values are thought to be accurate generally to within about a factor of 2–3 if the distance is accurately known (Knapp and Morris 1985). It is unlikely that the distances to the nearby Mira variables listed in Table 1 are in error by more than a factor of 2 (see Bowers and Hagen 1984), suggesting that the CO mass-loss rates are probably accurate to within factors of 5–10. For stars where CO mass-loss rates are not available, we have used mass-loss rates determined from the optical depth of the 10 μm silicate feature, from infrared luminosity and envelope expansion velocity, or from the size of the OH maser region. Uncertainties in the infrared values of the mass-loss rates are assumed to be similar to those estimated from CO, although it is difficult to assess their errors.

A plot of the outer radius of the H_2O maser region as a function of the mass-loss rate is shown in Figure 2. From theoretical considerations, such a relation has been proposed by Deguchi (1977) and by Cooke and Elitzur (1985), although the model of Deguchi places the H_2O masers much closer to the star than does that of Cooke and Elitzur. Based on a subset of the stars in Figure 2, Bowers (1985) also suggested that the size of the H_2O maser region increases with increasing mass-loss rate.

Figure 2 indeed shows such a trend, although there is considerable scatter for the stars with mass-loss rates $\sim 10^{-6}\ M_\odot\ yr^{-1}$. Nevertheless, Figure 2 (and Table 1) illustrate that small linear diameters of the H_2O maser region are found for nearby, optically identifiable Mira variables with small infrared excesses. Optically faint Miras which are bright infrared sources (i.e., IK Tau) have larger H_2O emission regions. The largest emission regions are associated with supergiant stars which have large infrared excesses indicative of high mass-loss rates. In this sense the value of the linear diameter for the H_2O emission from S Per ($\sim$300 AU; Diamond *et al.* 1987*a*) is intermediate between the largest known value for a Mira variable ($\sim$108 AU for IK Tau) and that for the supergiant NML Cyg ($\sim$720 AU), consistent with the "intermediate" mass-loss rate in Table 1. The OH luminosity of S Per also suggests an intermediate mass-loss rate (Bowers 1981). The scatter evident in Figure 2 may, to some extent, reflect the different methods of determining the mass-loss rate, as is apparent if, for example, we exclude the open circles which correspond to infrared mass-loss rates determined by Gehrz and Woolf (1971). Additional star-to-star differences in the environments of the circumstellar envelopes can also contribute to the scatter. An example may be *o* Ceti (Mira). If the CO mass-loss rate is correct, the radius of the H_2O maser region is smaller than is typical for other stars. This is particularly interesting because the SiO, H_2O, and OH luminosities for this star are significantly smaller than

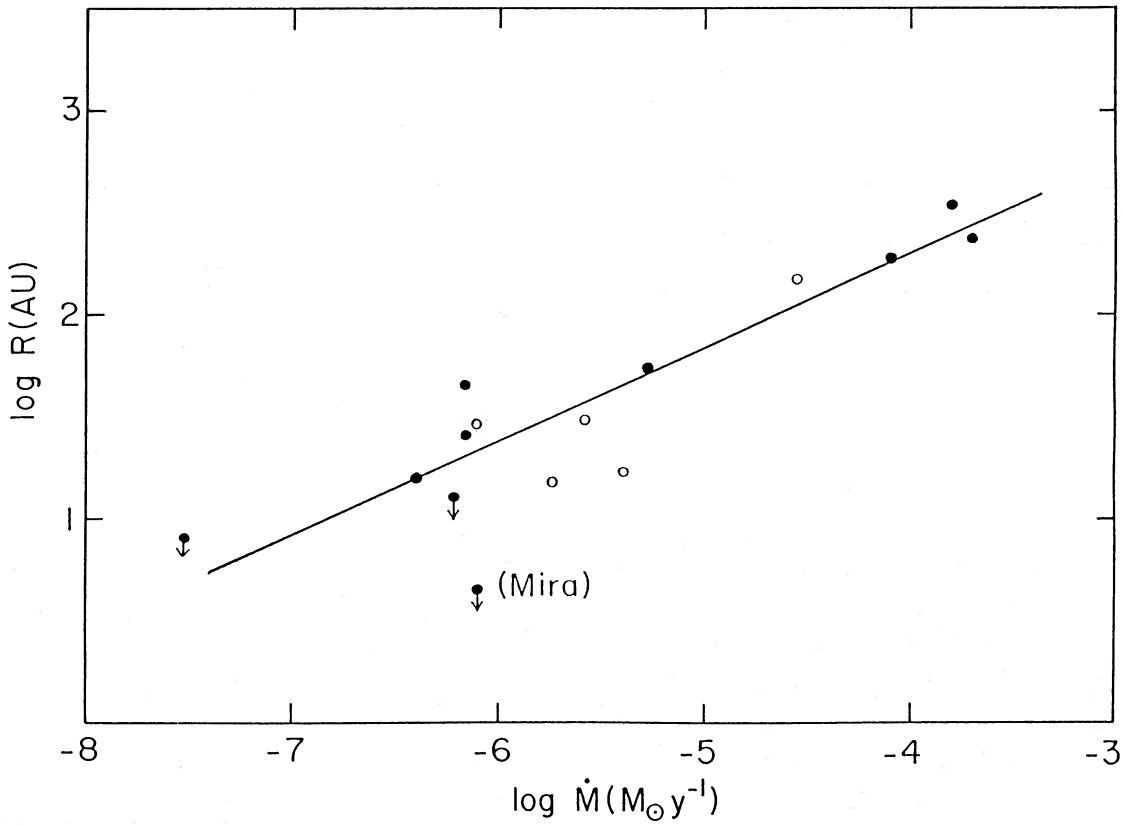

FIG. 2.—Maximum radius (in AU) of the H_2O maser regions as a function of the stellar mass-loss rate (in $M_\odot\ yr^{-1}$). *Open circles:* mass-loss rates determined by Gehrz and Woolf (1971). *Filled circles:* all other estimates in Table 1. *Solid line:* least squares fit to the data (excluding the three sources shown as upper limits).

for other Miras with mass-loss rates $\sim 10^{-6}\ M_\odot\ \mathrm{yr}^{-1}$ (Lane 1982; Bowers and Hagen 1984). These anomalies could be due to the presence of the blue subdwarf companion which may be causing photodissociation of molecules in the circumstellar envelope of Mira. Alternatively, the CO mass-loss rate may be significantly overestimated (see Knapp and Morris 1985). The H_2O luminosity suggests a mass-loss rate $\sim 10^{-8}\ M_\odot\ \mathrm{yr}^{-1}$ (Bowers and Hagen 1984), in which case our upper limit for the radius of the H_2O maser region may be close to the value indicated by the trend in Figure 2.

A least-squares fit (*solid line*) to all the points in Figure 2 except the three which indicate upper limits yields

$$\log R(\mathrm{AU}) = 0.46 \log \dot{M}(M_\odot\ \mathrm{yr}^{-1}) + 4.17\ , \qquad (1)$$

with a correlation coefficient of 0.91. The slope of the relationship is similar to that found for OH masers (Bowers *et al.* 1983), indicating that to first order both masers are produced in regions whose density is relatively constant from star to star (see Bowers 1985). For H_2O, we note that the above coefficients are only marginally different from those expected for a spherical envelope expanding at a characteristic velocity of 10 km s^{-1} with a total density $n(H_2) = 10^7$ cm^{-3} in the H_2O maser region. The trend in Figure 2 is in good agreement with the range of sizes predicted in the pumping model of Cooke and Elitzur (1985) for the indicated range of mass-loss rates. Their model is also supported by the correlation of mass-loss rate and H_2O maser luminosity discussed by Bowers and Hagen (1984).

IV. IK TAU

The star IK Tau has an exceptionally rich H_2O maser spectrum, with many features spanning a total velocity range of 41 km s^{-1}. This star is now discussed in detail. As an aid to interpreting our results, we present data in the following tables and figures relative to the stellar velocity. We do not use the H_2O emission to determine the stellar velocity because the width and shape of H_2O profiles from Mira variables are known to vary significantly with time (Schwartz, Harvey, and Barrett 1974; Cox and Parker 1979; Berulis *et al.* 1983). Instead, we adopt as the stellar velocity the mean velocity determined from the outer peaks of the doubly peaked OH emission profile at 1612 MHz since this is known to be a reliable velocity indicator for most OH/IR stars (Reid *et al.* 1977; Bowers *et al.* 1983). The adopted stellar velocity is thus $V_* = 34 \pm 0.5$ km s^{-1} for IK Tau (see profile of Silverglate *et al.* 1979). This is in good agreement with the value of 34.6 ± 0.4 km s^{-1} determined from CO emission (Knapp and Morris 1985).

Fifty-one channel maps show detectable maser emission. Each channel map shows from one to five maser spots or features which in some cases are easily distinguishable and in other cases appear to be spatially blended. Channel maps which show a small number of features (1, 2, or 3) tend to be those near the stellar velocity ($|V - V_*| \leq 5$ km s^{-1}) and those at the extreme velocity ends of the spectrum. Channel maps showing as many as four or five distinct emission spots occur at values of $(V - V_*)$ between 5 and 10 km s^{-1} and between -10 and -13 km s^{-1}.

Rather than present all 51 channel maps, a few sample maps along with the spectrum of IK Tau are displayed in Figure 3 to illustrate various characteristics of the data. The restoring beam for these CLEANed maps was a circular Gaussian of HPBW 0.″07. Figure 3*a* shows the spectrum marked with the stellar velocity and with the velocities of the maps displayed in Figures 3*b*–3*g*. Maps of the emission at the extreme velocity ends of the spectrum are shown in Figures 3*b* and 3*g*. Figure 3*b* shows a single unresolved maser spot at the extreme blue-shifted end of the spectrum ($V - V_* = -16.5$ km s^{-1}); this feature is near the edge of the feature which peaks at $V - V_* = -15.5$ km s^{-1} and occurs within 15 milliarcseconds (mas) of the center of the overall distribution of maser spots (see below). Figure 3*g* at $V - V_* = 13.8$ km s^{-1} shows a distribution of emission which is interpreted as three unresolved, spatially blended features. Another example of blended features is shown in Figure 3*e* ($V - V_* = 5.9$ km s^{-1}); the eastern emission clump in this map is interpreted as consisting of three blended features. Figure 3*f* ($V - V_* = 9.2$ km s^{-1}) shows emission from an inhomogeneous or clumpy ring; this distribution has been decomposed into four features (the SW component being a blend of two features). Figure 3*d* ($V - V_* = -2.7$ km s^{-1}) outlines further (half of) the low and intermediate velocity shell or ring of features seen in Figure 3*f*. Figure 3*c* ($V - V_* = -7.3$ km s^{-1}) consists of two features; the one to the northwest is the emission spot farthest from the center of the overall maser distribution (see Fig. 4). It must be emphasized that intercomparison of the maps in several adjacent channels is essential to the decomposition process. The manner of determining positions of features is described in more detail below.

None of the channel maps show unambiguous evidence for resolved (extended) emission. By detailed comparison of maps in adjacent channels, it can be shown that emission which appears to be extended in one channel map is more likely to be (or at least is consistent with) a blend of discrete unresolved maser features whose separate existence may be more evident in a neighboring channel, where one or more of the blended features has disappeared. A list of 31 maser features was extracted from the 51 maps by comparing the appearance of the emission at the same spatial position on maps in adjacent velocity channels. To define a feature, we require that the emission appears on at least one adjacent map at a position within 0.″01. Total line widths (i.e., FWZP) of features range from 2 to 10 channels (1.3–6.6 km s^{-1}). Due to the spatial blending of many of the features and limited dynamic range on maps with strong features, it is difficult to determine peak flux densities of individual features on each map and hence accurate half-power linewidths.

Table 2 lists the 31 maser features. Column (1) gives the velocity of the feature relative to the LSR, column (2) lists the velocity of the feature relative to the stellar velocity, and column (3) gives the peak flux density. Columns (4) and (5) give the position offsets in milliarseconds relative to the $V - V_* = -15.5$ km s^{-1} feature. The accuracy of the relative positions is estimated to be 5 mas.

For presentation purposes, the features have been divided into two groups: those with low relative velocities ($|V - V_*| \leq 9$ km s^{-1}) and those with high relative velocities ($|V - V_*| \geq 9$ km s^{-1}). Separate maps of the low- and high-velocity features are shown in Figure 4. The most striking aspect of the low velocity emission distribution is a ringlike appearance; there are no low-velocity features in the central region of the map. Furthermore, the map shows a high degree of circular symmetry. The maser spots are confined to a region $\sim 0.''33$ in diameter (89 AU at a distance of 270 pc). The high-velocity features, on the other hand, are not concentrated in the central regions (as would be expected for a spherical expanding shell) but show an elongated, somewhat flattened distribution of

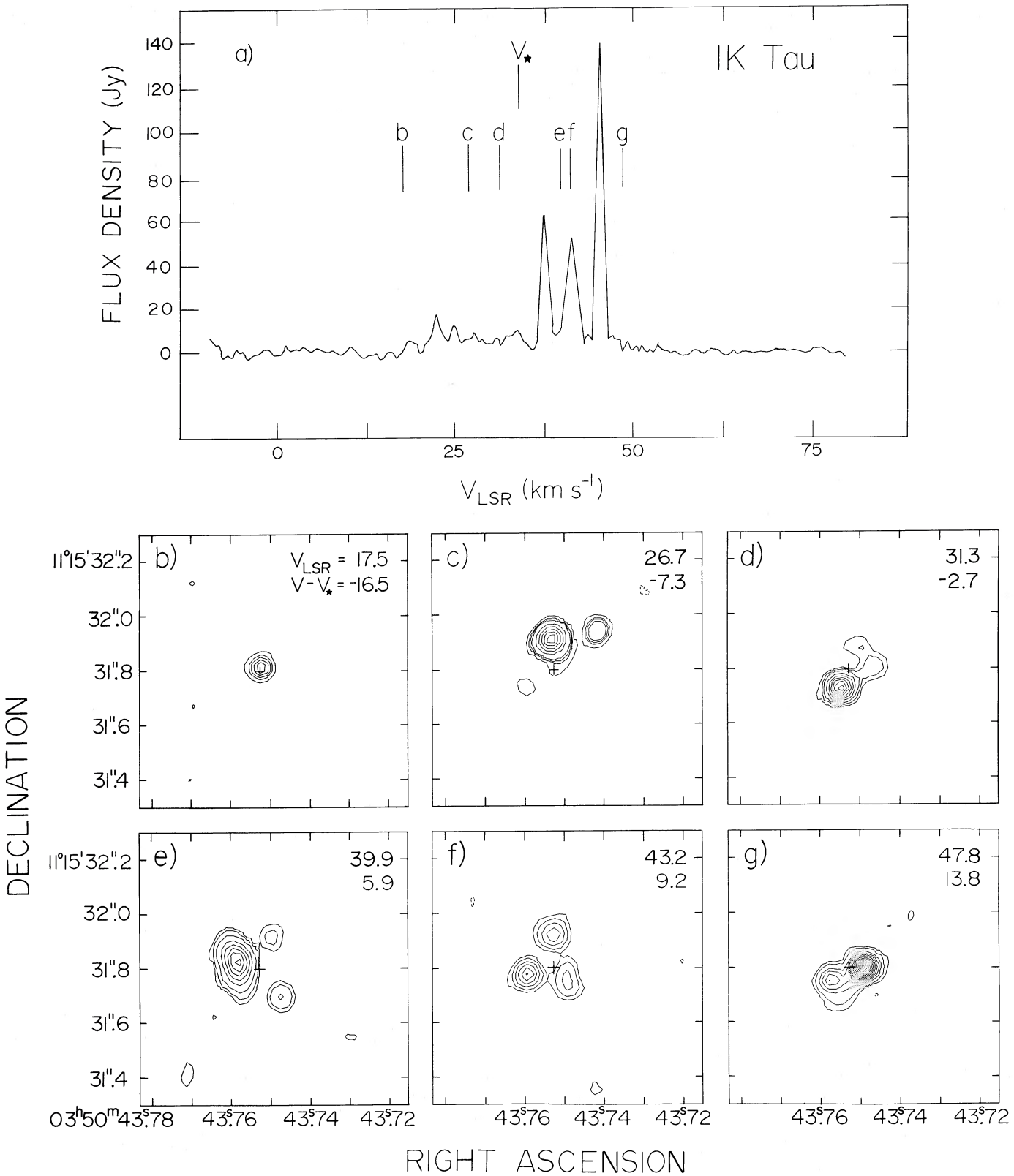

FIG. 3.—(*a*) Onsala H_2O spectrum of IK Tau obtained on 1983 October 9. Parameters are as in Fig. 1. (*b–g*) A sample of six of the 51 CLEANed channel maps of H_2O maser emission from IK Tau. Lowest (positive) contour on each map is at the 3 σ level ($\sim$0.2 Jy per beam). Restoring beam was a circular Gaussian of HPBW 0".07. Cross on each map marks the assumed stellar position (*see text*). Radial velocity with respect to the LSR and velocity relative to the stellar velocity are shown in the upper right-hand corner of each map. (*b*) The peak flux density is 0.69 Jy per beam. The contour levels are −0.2, 0.2, 0.3, 0.4, 0.5, and 0.6 Jy per beam. (*c*) Peak flux density is 3.1 Jy per beam. Contour levels are −0.2, 0.2, 0.3, 0.4, 0.5, 1.0, 1.5, 2.0, and 3.0 Jy per beam. (*d*) Peak flux density is 2.5 Jy per beam. Contour levels are −0.2, 0.2, 0.3, 0.5, 0.8, 1.1, 1.4, 1.7, 2.0, and 2.3 Jy per beam. (*e*) Peak flux density is 6.4 Jy per beam. Contour levels are −0.3, 0.3, 0.5, 1.0, 2.0, 3.0, 4.0, 5.0, and 6.0 Jy per beam. (*f*) Peak flux density is 1.1 Jy per beam. Contour levels are −0.2, 0.2, 0.3, 0.5, 0.7, 0.9, and 1.1 Jy per beam. (*g*) Peak flux density is 2.6 Jy per beam. Contour levels are −0.2, 0.2, 0.3, 0.6, 0.8, 1.0, 1.2, 1.4, 1.6, 1.8, 2.0, 2.2, and 2.4 Jy per beam.

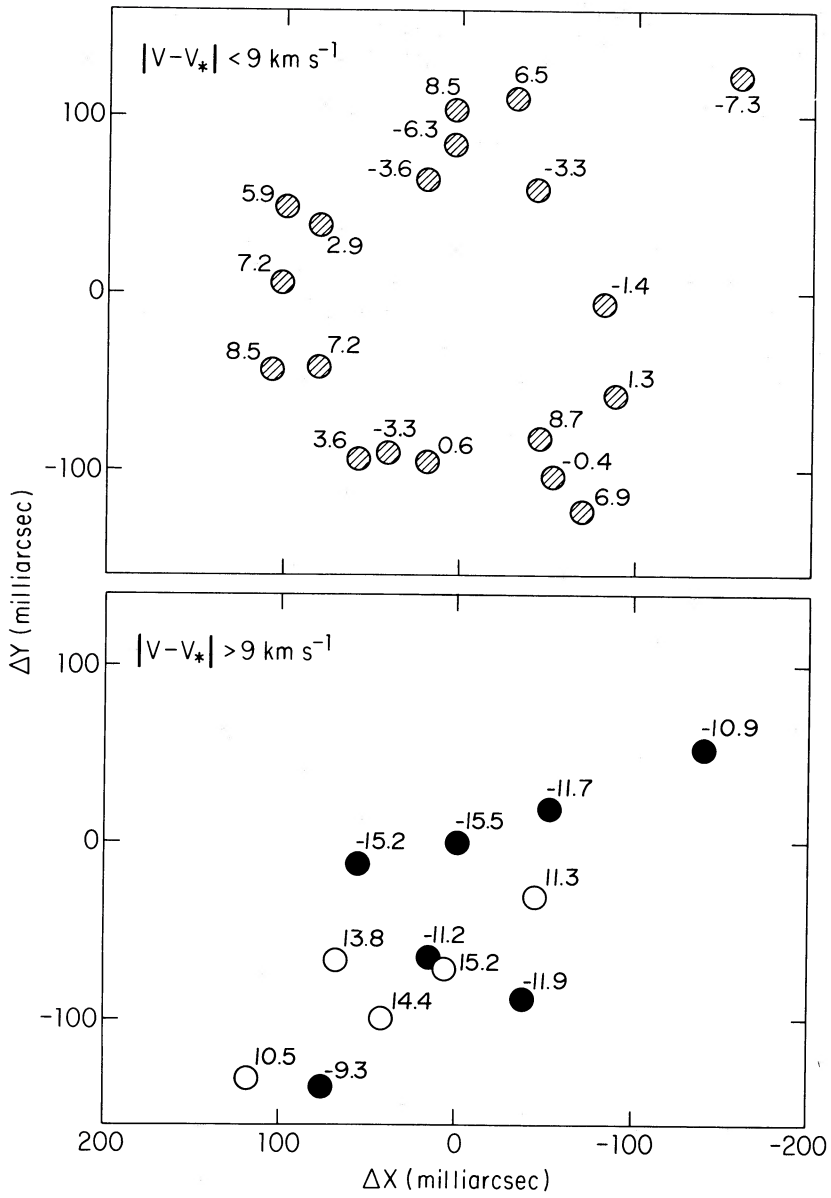

FIG. 4.—Maps of the H_2O maser features toward IK Tau. Maser spots are labeled with their velocities (in km s^{-1}) relative to the stellar velocity. *Top:* crosshatched circles represent positions of low-velocity features ($|V-V_*| \leq 9$ km s^{-1}). *Bottom:* filled circles represent positions of extreme blueshifted features ($V-V_* \leq -9$ km s^{-1}) and open circles represent extreme redshifted features ($V-V_* \geq 9$ km s^{-1}). The (0, 0) positions on both maps corresponds to the feature at $(V-V_*) = -15.5$ km s^{-1} (see Table 2).

roughly the same extent as the low-velocity features. The centroid of the high-velocity features is located somewhat to the south of the geometric center defined by the ringlike distribution of low-velocity features.

The optical and infrared positions of IK Tau are not known with sufficient accuracy to provide independent evidence for the location of the star on our H_2O maser maps. However, because of the symmetry evident in the distribution of the low-velocity masers in Figure 4, we believe we can infer the stellar position quite accurately. In the analysis which follows, we have taken the geometrical center of the "hole" in the low-velocity maser distribution to be the stellar position. This position is 15 mas south of the highest velocity (blueshifted) maser feature observed. In order to investigate the kinematics of the gas in the H_2O maser region, we computed the angular distance of each maser feature listed in Table 2 from the assumed stellar position. The distances are plotted as a function of $V-V_*$ in Figure 5. The distribution of features shown in Figure 5 is not consistent with a model consisting of a single spherical shell expanding at a constant velocity. Such models have been shown to adequately describe several of the 1612 MHz OH maser clouds associated with OH/IR stars (see Bowers *et al.* 1983; Chapman *et al.* 1984; Herman *et al.* 1985). Instead, we have chosen to fit subsets of the IK Tau data with shells of varying radii. For a constant velocity of expansion, the angular radius a of a maser feature as a function of its observed radial velocity ($V-V_*$) is given by

$$a(V-V_*) = A\{1-[(V-V_*)/V_{\rm exp}]^2\}^{1/2} \quad (2)$$

where A is the radius of the maser shell and $V_{\rm exp}$ is the expan-

TABLE 2

RELATIVE POSITIONS OF H_2O MASER FEATURES IN IK TAU

V_{lsr} (km s^{-1}) (1)	$V-V_*$ (km s^{-1}) (2)	I_{peak} (Jy per beam) (3)	Δx (mas) (4)	Δy (mas) (5)
18.5.....	−15.5	1.8	0	0
18.8.....	−15.2	2.9	56	−12
22.1.....	−11.9	1.4	−38	−88
22.3.....	−11.7	8.1	−53	19
22.8.....	−11.2	1.6	16	−65
23.1.....	−10.9	2.6	−140	53
24.7.....	−9.3	7.8	76	−138
26.7.....	−7.3	0.8	−158	123
27.7.....	−6.3	4.8	4	84
30.4.....	−3.6	0.8	20	64
30.7.....	−3.3	1.0	−43	−59
30.7.....	−3.3	2.8	41	−90
32.6.....	−1.4	3.9	−81	−5
33.6.....	−0.4	5.1	−53	−103
34.6.....	0.6	1.1	19	−95
35.3.....	1.3	0.7	−88	−57
36.9.....	2.9	1.4	80	38
37.6.....	3.6	42.1	57	−93
39.9.....	5.9	~1.2	99	49
40.5.....	6.5	1.3	−31	110
40.9.....	6.9	6.1	−69	−123
41.2.....	7.2	27.1	80	−42
41.2.....	7.2	~10.0	101	6
42.5.....	8.5	1.5	4	103
42.5.....	8.5	~10.0	107	−43
42.7.....	8.7	0.5	−45	−82
44.5.....	10.5	2.7	118	−133
45.3.....	11.3	98.5	−45	−31
47.8.....	13.8	1.2	68	−67
48.4.....	14.4	0.9	42	−99
49.2.....	15.2	1.0	7	−71

sion velocity. Assuming an expansion velocity of 15.5 km s^{-1}, separate least squares fits were made to the data represented in Figure 5 by filled and open circles. The resulting shell radii are 93 mas (25 AU) and 218 mas (59 AU). The redshifted features represented by plus signs in Figure 5 were excluded from the fits because of their anomalous position on the plot. These features, as well as the generally clumpy distribution of the emission (see Figs. 3*b*–3*g*), suggest that density inhomogeneities and turbulent motions of several km s^{-1} may be important in the H_2O maser regions. For comparison, the expansion velocity in the OH maser region, presumably located at larger distance from the star, is 16.7 km s^{-1} (Herman and Habing 1985).

V. R AQL

The only other giant star we observed which showed more than ~3 maser features spread over an area greater than one or two VLA beams in the Mira variable R Aql. Maps of the H_2O maser emission from this star were previously obtained with the VLA in 1981 January and 1982 March by JSB, at which times the star was at visual phase 0.99 and 0.55, respectively. The data presented by JSB show significant changes from one epoch to the next in both the velocity and spatial structure of the maser emission. In particular, the observations near minimum phase (1982 March) show the maser region to have approximately twice the spatial extent observed near maximum (1981 January), although this result must be regarded with caution since limited dynamic range on the maps from the earlier epoch may have prevented detection of low-level emission.

In the present experiment (1983 October), R Aql was at visual phase 0.69 (J. Mattei, private communication). Maser emission was detected over the velocity range 43.3–49.9 km s^{-1}, similar to that observed in the 1981 observations ($\Delta v = 6.9$ km s^{-1}) but somewhat smaller than the velocity extent of the emission in 1982 ($\Delta v = 12$ km s^{-1}). The peak flux density (see Fig. 1) is 24 Jy, about half the peak intensity observed in 1982 March and about one-eighth the peak intensity in 1981 January. Peak emission occurs at a velocity of ~48 km s^{-1} at all three epochs. The stellar velocity of R Aql as determined from the double-peaked OH maser profile is 47.4 km s^{-1} and the circumstellar expansion velocity in the 1612 MHz OH maser region is 8.2 km s^{-1} (Bowers *et al.* 1983).

As indicated in Table 1, the channel maps show ~13 discrete features distributed over a region 0".33 (57 AU) in size. Figure 6 presents a map of the H_2O features marked with their velocities relative to the stellar velocity. The map shows a remarkably elongated distribution of maser spots, with a length-to-width ratio of ~6.4. Simple kinematic patterns such as rotation or constant velocity expansion/contraction are not evident from the data. Velocities within 1 km s^{-1} of the stellar velocity are seen both near the center of the map and at the extremities of the distribution. Since velocities as high as 3.4 km s^{-1} (relative to V_*) are also observed, this suggests that one or both of the following statements are true: (1) turbulent or streaming motions of H_2O maser clumps must be at least 2–3 km s^{-1} and (2) radial acceleration of gas is occurring across the H_2O maser region. The size of the 1612 MHz OH emission region of R Aql, where the gas has presumably reached terminal expansion velocity, is larger by a factor of ~24 than the H_2O maser region (Bowers *et al.* 1983).

Comparison of the map in Figure 6 with the earlier maps of JSB is complicated by the time variability of the emission as well as by possible differences in the dynamic range of the maps. The 1982 map shows a similarly elongated distribution, while the 1981 map near maximum phase shows a smaller, less elongated distribution. Although nonspherical geometry and a lack of simple kinematic patterns appear to be present in the H_2O maser region of R Aql, further observations are required before the structure and kinematics of the circumstellar envelope of this source can be understood in detail.

VI. SUMMARY

Measurements of the spatial extent of the H_2O emission from giant and supergiant long-period variable stars confirm that there is a correlation between the overall size of the maser region and the stellar mass-loss rate. A similar relationship has previously been found for the OH masers associated with these stars.

The spatial structure of the H_2O maser regions toward 12 stars has been presented. For most of the stars studied, the maser emission was found to originate from one to four maser spots. The Mira variable IK Tau exhibited an exceedingly rich spectrum containing ~31 features. The spatial distribution of these features is consistent with a double expanding shell geometry of stellar water masers. A model consisting of two spherical shells of radii 25 and 59 AU, both expanding at a velocity of 15.5 km s^{-1}, provides a reasonable fit to the data. There is also evidence for density clumping and velocity inhomogeneities in IK Tau's circumstellar envelope.

The H_2O maser emission region of the Mira variable R Aql is highly elongated and provides evidence for turbulent velo-

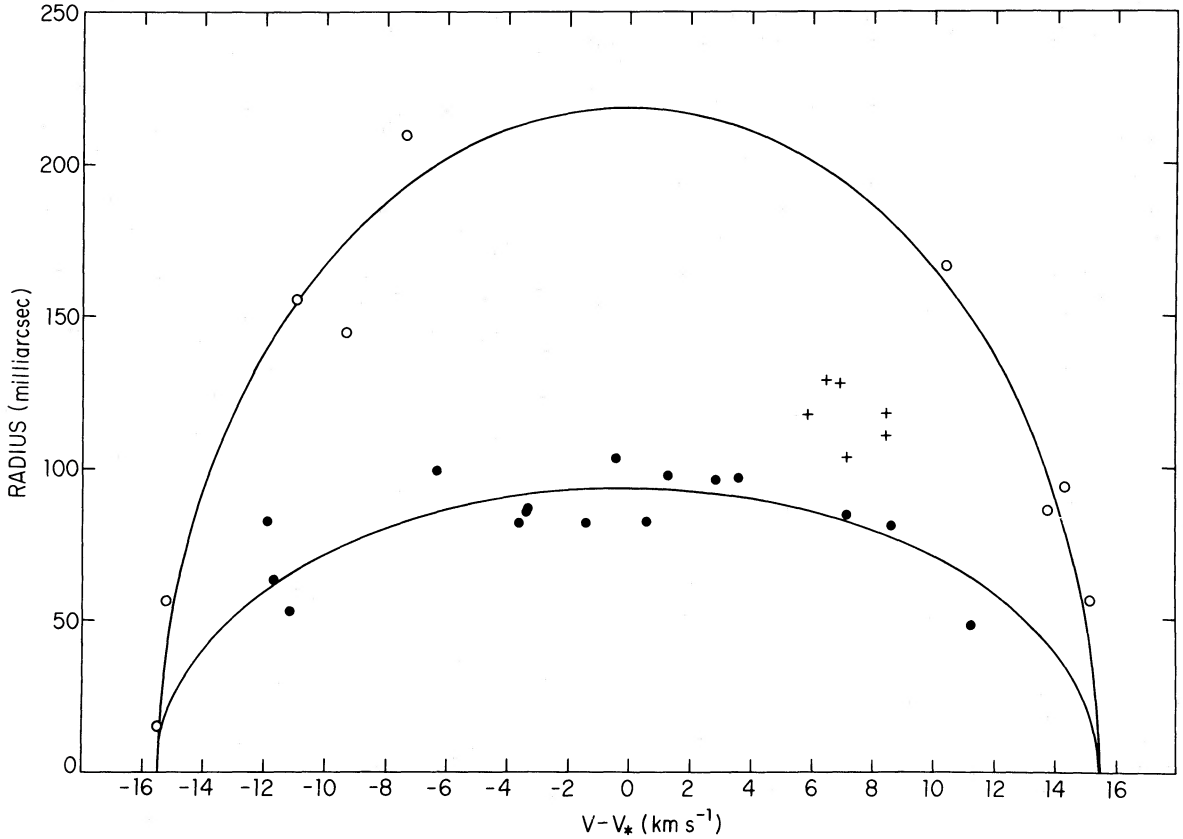

FIG. 5.—Angular radius (in milliarseconds) of H_2O maser features toward IK Tau as a function of velocity relative to the stellar velocity. *Solid curves:* least-squares fits of eqn. (2) to subsets of the data; upper curve was fitted to the open circles, the lower curve was fitted to the filled circles. Maser features represented by pluses were excluded from both fits (*see text*).

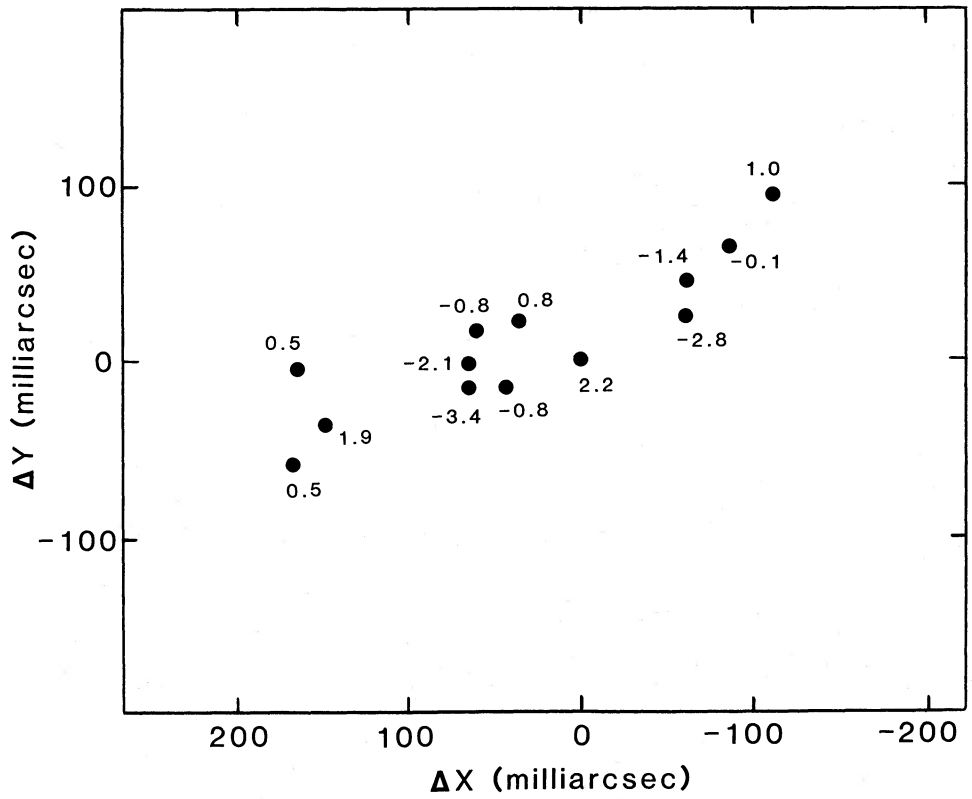

FIG. 6.—Map of the H_2O maser features toward R Aql obtained 1983 October 6–7. Maser spots are labeled with their velocities (in km s^{-1}) relative to the stellar velocity.

cities of ~ 2–3 km s^{-1} or radial acceleration of gas (or both) in the maser region.

We would like to thank L.-A. Nyman for his help in obtaining the single-dish spectra. Onsala Space Observatory is run by Chalmers University of Technology with financial support from the Swedish Natural Science Research Council. We gratefully acknowledge the AAVSO observational data sent to us by the director, Janet A. Mattei.

REFERENCES

Armandroff, T. E., and Herbst, W. 1981, *A.J.*, **86**, 1923.
Berulis, I. I., Lekht, E. E., Pashchenko, M. I., and Rudnitskii, G. M. 1983, *Soviet Astr.*, **27**, 179.
Bowers, P. F. 1981, *A.J.*, **86**, 1930.
———. 1985, in *Mass Loss from Red Giants*, ed. M. Morris and B. Zuckerman (Dordrecht: Reidel), p. 189.
Bowers, P. F., and Hagen, W. 1984, *Ap. J.*, **285**, 637.
Bowers, P. F., Johnston, K. J., and Spencer, J. H. 1983, *Ap. J.*, **274**, 733.
Celis, S. L. 1980, *Astr. Ap.*, **89**, 145.
———. 1981, *Astr. Ap.*, **99**, 58.
Chapman, J. M., and Cohen, R. J. 1986, *M.N.R.A.S.*, **220**, 513.
Chapman, J., Cohen, R. J., Norris, R. P., Diamond, P. J., and Booth, R. S. 1984, *M.N.R.A.S.*, **207**, 149.
Cooke, B., and Elitzur, M. 1985, *Ap. J.*, **295**, 175.
Cox, G. G., and Parker, E. A. 1979, *M.N.R.A.S.*, **186**, 197.
Deguchi, S. 1977, *Pub. Astr. Soc. Japan*, **29**, 669.
Diamond, P. J., Johnston, K. J., Chapman, J. M., Lane, A. P., Bowers, P. F., Spencer, J. H., and Booth, R. S. 1987*a*, *Astr. Ap.*, **174**, 95.
Diamond, P. J., *et al.* 1987*b*, in preparation.
Gehrz, R. D., and Woolf, N. J. 1971, *Ap. J.*, **165**, 285.
Herman, J., Baud, B., Habing, H. J., and Winnberg, A. 1985, *Astr. Ap.*, **143**, 122.
Herman, J., and Habing, H. J. 1985, *Astr. Ap. Suppl.*, **59**, 523.
Humphreys, R. M. 1975, *Pub. Astr. Soc. Pac.*, **87**, 433.
Hyland, A. R., Becklin, E. E., Frogel, J. A., and Neugebauer, G. 1972, *Astr. Ap.*, **16**, 204.
Johnston, K. J., Spencer, J. H., and Bowers, P. F. 1985, *Ap. J.*, **290**, 660 (JSB).
Knapp, G. R., and Morris, M. 1985, *Ap. J.*, **292**, 640.
Knapp, G. R., Phillips, T. G., Leighton, R. B., Lo, K. Y., Wannier, P. G., Wootten, H. A., and Huggins, P. J. 1982, *Ap. J.*, **252**, 616.
Lane, A. P. 1982, Ph.D. thesis, University of Massachusetts.
———. 1984, in *IAU Symposium 110, VLBI and Compact Radio Sources*, ed. R. Fanti, K. Kellerman, and G. Setti (Dordrecht: Reidel), p. 329.
Lockwood, G. W., and Wing, R. F. 1982, *M.N.R.A.S.*, **198**, 385.
Morris, M., Redman, R., Reid, M. J., and Dickinson, D. F. 1979, *Ap. J.*, **229**, 257.
Reid, M. J., Muhleman, D. O., Moran, J. M., Johnston, K. J., and Schwartz, P. R. 1977, *Ap. J.*, **214**, 60.
Schwartz, P. R., Harvey, P. M., and Barrett, A. H. 1974, *Ap. J.*, **187**, 491.
Silverglate, P., Zuckerman, B., Terzian, Y., and Wolff, M. 1979, *A.J.*, **84**, 345.
Spencer, J. H., Johnston, K. J., Moran, J. M., Reid, M. J., and Walker, R. C. 1979, *Ap. J.*, **230**, 449.
Wannier, P. G., Leighton, R. B., Knapp, G. R., Redman, R. O., Phillips, T. G., and Huggins, P. J. 1979, *Ap. J.*, **230**, 149.
Wilson, W. J., Schwartz, P. R., Neugebauer, G., Harvey, P. M., and Becklin, E. E. 1972, *Ap. J.*, **177**, 523.
Zuckerman, B., and Dyck, H. M. 1986, *Ap. J.*, **304**, 394.

P. F. BOWERS, K. J. JOHNSTON, and J. H. SPENCER: Code 4130, Naval Research Laboratory, Washington, DC 20375

P. J. DIAMOND: Max-Planck-Institute für Radioastronomie, Auf dem Hügel 69, D-5300 Bonn 1, West Germany

ADAIR P. LANE: Astronomy Department, Boston University, 725 Commonwealth Avenue, Boston, MA 02215